Special Collection

IMPACTS

An Airborne Multifrequency Microwave Analysis of Precipitation within Two Winter Cyclones

AMANDA RICHTER[a] AND TIMOTHY J. LANG[b]

[a] *University of Alabama in Huntsville, Huntsville, Alabama*
[b] *NASA Marshall Space Flight Center, Huntsville, Alabama*

ABSTRACT: NASA's Investigation of Microphysics and Precipitation for Atlantic Coast-Threatening Snowstorms (IMPACTS) field campaign gathered data using "satellite-simulating" (albeit with higher-resolution data than satellites currently provide) and in situ aircraft to study snowstorms, with an emphasis on banding. This study used three IMPACTS microwave instruments—two passive and one active—chosen for their sensitivity to precipitation microphysics. The 10–37-GHz passive frequencies were well suited for detecting light precipitation and differentiating rain intensities over water. The 85–183-GHz frequencies were more sensitive to cloud ice, with higher cloud tops manifesting as lower brightness temperatures, but this did not necessarily correspond well to near-surface precipitation. Over land, retrieving precipitation information from radiometer data is more difficult, requiring increased reliance on radar to assess storm structure. A dual-frequency ratio (DFR) derived from the radar's Ku- and Ka-band frequencies provided greater insight into storm microphysics than reflectivity alone. Areas likely to contain mixed-phase precipitation (often the melting layer/bright band) generally had the highest DFR, and high-altitude regions likely to contain ice usually had the lowest DFR. The DFR of rain columns increased toward the ground, and snowbands appeared as high-DFR anomalies.

SIGNIFICANCE STATEMENT: Winter precipitation was studied using three airborne microwave sensors. Two were passive radiometers covering a broad range of frequencies, while the other was a two-frequency radar. The radiometers did a good job of characterizing the horizontal structure of winter storms when they were over water, but struggled to provide detailed information about winter storms when they were over land. The radar was able to provide vertically resolved details of storm structure over land or water, but only provided information at nadir, so horizontal structure was less well described. The combined use of all three instruments compensated for individual deficiencies, and was very effective at characterizing overall winter storm structure.

1. Introduction

a. Background

Winter weather can cause immense disruption to infrastructure, economic activity, and daily life. The Investigation of Microphysics and Precipitation for Atlantic Coast-Threatening Snowstorms (IMPACTS) is a multiyear field campaign dedicated to studying winter storms, particularly those that exhibit banded structures, along the east coast and in the central United States (McMurdie et al. 2022). The science goals of IMPACTS

are to characterize snowbands in U.S. winter storms; to understand processes that produce these precipitation structures; and to use this information to improve remote sensing and modeling of snowfall.

It is well documented that the precipitation within the comma head of a winter cyclone is commonly organized into narrow convective generating cells within broader stratiform precipitation (Rauber et al. 2014; Ramelli et al. 2021). A generating cell is characterized as a small region of enhanced radar reflectivity with a trail of enhanced reflectivity (a fallstreak) below, indicative of falling hydrometeors (Ramelli et al. 2021). Generating cells are believed to be sites of ice crystal growth, where the latent heat released from ice nucleation and growth can contribute to the maintenance of the cell (Keeler et al. 2016).

A case study from the Profiling of Winter Storms (PLOWS) field campaign identified seeder–feeder processes initiated by generating cells enhancing precipitation rate on the cold side

of the comma head (Rauber et al. 2014), while other studies have found generating cells across the entirety of comma heads in multiple cyclones (Rosenow et al. 2014). Such cells have been observed reaching several kilometers above ground level (Stark et al. 2013) with seeder–feeder interactions being common (Misumi et al. 2021; Rutledge and Hobbs 1984; Ramelli et al. 2021), including in low-level or warm process environments (Hobbs et al. 1980; Herzegh and Hobbs 1980).

The analysis of seeder–feeder regions in Ramelli et al. (2021) demonstrated great spatial and temporal variance in ice crystal habits and riming. Pristine ice crystals and heavily rimed ice were likely to be generated or experience significant growth in seeder–feeder regions. In addition, a mixed-phase cloud, which transitioned from liquid to ice, was observed, with the Wegener–Bergeron–Findeisen processes deemed a likely contributor to its glaciation (Ramelli et al. 2021).

Numerous microphysical and thermodynamical processes also occur within and across the melting layer or radar-indicated bright band. For instance, diabatic heating from the change in phase from ice to water has been found to alter the thermal character around the location of melting, cooling the area in particular (Carlin and Ryzkov 2019).

A 2015 study found that aggregation is largely responsible for particle growth between $-4°$ and $+1°C$, and melting can be inhibited by sufficiently dry conditions (Heymsfield et al. 2015). Li et al. (2020) suggested that riming may suppress aggregation at the top of a melting layer. This study also found that the rapid freezing of supercooled water drops onto ice crystals (riming) can mitigate sagging in the melting layer in light precipitation, while it exacerbates sagging in moderate to heavy precipitation. Although airborne in situ instruments can directly gather microphysical and dynamical information from a melting layer (Heymsfield et al. 2015), large-scale, everyday use of such instruments is not feasible. Unfortunately, small changes in snow microphysics also can substantially impact millimeter-wave radar observations (Li and Moisseev 2019).

Thus, the microphysical environment is highly variable within comma-head precipitation, complicating any interpretation of remote sensing instrument retrievals. In Stark et al. (2013), the passage of a precipitation band was observed to feature light riming on predominantly needle-type crystals before the passage of a precipitation band, with an increase in riming as the band approached the observation site. Variable riming on dendrites was observed within the mature snowband, while platelike crystals were observed after its passage. Generating-cell cloud tops were found to reach several kilometers above ground level.

b. Science goals of this study

Precipitation within the comma head is complex and difficult to characterize without prior knowledge of hydrometeor particle size distributions. The objective of this paper is to assess observations, made by active and passive microwave instruments used in the IMPACTS field campaign, that characterize cloud and precipitation features. The Global Precipitation Measurement (GPM) core observatory is one of the most well-known precipitation satellites today. It was engineered to be the centerpiece of a constellation of precipitation satellites, improving upon predecessor satellites with the intent to advance knowledge regarding storm structure, precipitation microphysics, and natural hazard forecasting, among many other subjects (Hou et al. 2014). The GPM core observatory is equipped with active and passive microwave instruments. The passive GPM Microwave Imager (GMI) (Draper et al. 2015) is a multichannel conical-scanning radiometer featuring 13 channels which range in frequency between 10 and 183 GHz. The Dual-Frequency Precipitation Radar (DPR) is a Ku- and Ka-band precipitation radar, providing three-dimensional scans of precipitation across the planet (Hou et al. 2014).

This study will use three airborne microwave-frequency instruments that have very similar attributes to the GPM's active and passive sensors. The main consideration is how GPM-frequency instruments would return information on snowfall and rain at much higher spatial and temporal resolutions than is possible on the spaceborne platform. It is the goal to understand how these instruments observe microphysical structures and processes, where they struggle, and how combining their observations can aid in understanding precipitation bands in stratiform and convective environments. It is hypothesized that the range of radiometer frequencies used will be highly complementary. Low frequencies will likely provide more utility over water, and high frequencies will likely provide greater utility over land. The performance of the radiometers are expected to be largely dependent on surface emission properties, and the radar will provide crucial information over land unaffected by emission properties of the surface. If two radar frequencies are combined into a single product, it should prove valuable for identifying microphysically important processes, such as regions of probable ice growth. To obtain the most useful microphysical information from dual-frequency radar data, it is best for one frequency to satisfy the Rayleigh approximation while the other does not.

2. Instruments

a. AMPR

The Advanced Precipitation Microwave Radiometer (AMPR) is a cross-track-scanning passive radiometer that produces calibrated brightness temperatures (T_b) at 10.7, 19.35, 37.1, and 85.5 GHz, each with two orthogonal channels (A and B) whose scene polarization basis rotates with respect to the feedhorn polarization basis as a function of scan angle (Amiot et al. 2021). These frequencies are particularly sensitive to the emission and scattering of precipitation-size liquid water, ice, and cloud water, with the 85-GHz channel somewhat sensitive to water vapor (Spencer et al. 1994). The ground resolutions for AMPR's 10-, 19-, 37-, and 85-GHz frequencies are approximately 2.8 km, 2.8 km, 1.5 km, and 600 m, respectively, at a flight altitude of 20 km. AMPR was used in IMPACTS due to the similarity of its frequencies with those of the Global Precipitation Measurement (GPM) Microwave Imager (GMI), particularly those between 10.6 and 89 GHz. The ground resolutions for GPM's closest frequencies are 19.4 km × 32.2 km at 10 GHz, 11.2 km × 18.3 km at 18.7 GHz, and 8.6 km × 15.0 km at 36.5 GHz Hou et al. (2014).

AMPR has been used in past field campaigns including the Olympic Mountains Experiment (OLYMPEX) (Houze et al. 2017) and the Cloud, Aerosol, and Monsoon Processes, Philippines Experiment (CAMP²Ex) (Reid et al. 2023). Previous work with AMPR imagery has explored the ability to detect and distinguish various microphysical environments or dominant precipitation types within cloud and precipitation structures using all four channels in concert.

A combined active–passive retrieval analysis to associate multiparameter radar data and AMPR imagery with likely hydrometeor types and sizes found that 19-GHz brightness temperature fluctuations correlate with radar reflectivity near 3 km in altitude. It was also found that 19 GHz radiometrically saturates (i.e., the input signal's voltage exceeds what the instrument can measure) more readily than 10 GHz, and 10 GHz observes ground wetting as a temperature depression (Vivekanandan et al. 1993).

In observations of convective systems around Florida, retrievals of cloud and precipitation profiles over water could be done with AMPR alone, but required radar assistance over land (Olson et al. 1996). AMPR's lowest three frequencies were found useful in differentiating graupel from hail, while liquid precipitation was best retrieved by a hydrometeor-classification algorithm when underlying large ice particles (Leppert and Cecil 2015). AMPR has also shown some use in detecting storm structure, as McGaughey et al. (1996) detected a vertical tilt within a tropical squall line and hurricane eyewall, apparent as a spatial shift in AMPR's three higher frequencies' maximum brightness temperature depressions away from the maximum emission signature in 10 GHz. Amiot et al. (2021) demonstrated success with using AMPR T_b to retrieve integrated cloud liquid water, water vapor, and 10-m wind speed.

b. CoSMIR

The Conical Scanning Millimeter-wave Imaging Radiometer (CoSMIR) is a unique passive radiometer that operates at many channels, the central frequencies of which are 50.3 GHz, 52.8 GHz, 89.0 GHz with horizontal and vertical polarization (H and V), 165.5 GHz (H and V), 183.31 ± 1 GHz, 183.31 ± 3 GHz, and 183.31 ± 7 GHz (Kroodsma et al. 2019). CoSMIR was designed to match tropospheric sounding channels of the Defense Meteorological Satellite Program's Special Sensor Microwave Imager/Sounder (Piepmeier et al. 2002). CoSMIR's scan head is mounted on a dual-axis gimbaled mechanism, enabling a large variety of scan cycles (Kroodsma et al. 2019). The instrument can be programmed to scan conically, cross-track, or along-track, and is capable of performing hybrid scans, where a combination of scan methods are used. In this study, conical scans were used to generate swath images, and along-track scans were used to examine nadir brightness temperature. CoSMIR's ground footprint at nadir is 1.4 km × 1.4 km. The ground resolution for GPM's analogous channels is 4.4 km × 7.3 km (Hou et al. 2014).

CoSMIR has been used to support GPM algorithm development (Skofronick-Jackson and Wang 2012) and was flown over various storm structures in OLYMPEX (Kroodsma et al. 2019). Data from CoSMIR have also been used in combination with AMPR to assess the ability to identify dominant

hydrometeor types with radiometers that cover a frequency range similar to the GMI. Compared to hail, graupel is a relatively strong scatterer at high frequencies (such as 165 GHz from CoSMIR) and relatively weak scatterer at low frequencies (e.g., 19 GHz and lower) (Leppert and Cecil 2015). The same study also found that a particular range of brightness temperatures across the GMI range (19.4 GHz < 250 K, 37.1 GHz < 240 K, 89.0 GHz < 220 K, and 165.5 GHz < 140 K) indicates a likelihood for near-surface precipitation. While there is precedent for the use of multiple radiometers to assess in-cloud characteristics, studies focusing on winter storms in particular are sparse. This work is unique in that it utilizes AMPR and CoSMIR together in the context of winter cyclones.

c. HIWRAP

The High-Altitude Imaging Wind and Rain Airborne Profiler (HIWRAP) is a dual-frequency, dual-beam Ka- and Ku-band Doppler radar (Heymsfield et al. 2013; Jensen et al. 2016; Li et al. 2008, 2016; Tian et al. 2015). Its 14- and 34-GHz channels closely resemble those within the GPM DPR. Mounted onboard the "satellite-simulating" ER-2 aircraft, HIWRAP provides nadir curtain reflectivity imagery and wind field information within precipitation systems (Li et al. 2016; Tian et al. 2015). The beamwidths for Ku and Ka are 3° and ~1.2°, respectively, with respective ground footprints of 1000 and 400 m at an altitude of 20 km. The Ku- and Ka-band resolutions on GPM's DPR are 5 km Hou et al. (2014).

HIWRAP is calibrated in three steps, outlined in Li et al. (2016): 1) Use instrument component parameters to calculate the radar range equation detailed in Doviak and Zrnic (1993); 2) using the ocean surface return as an external reference [as in Li et al. (2005) and Tanelli et al. (2006)]; 3) internal calibration using a pulse-by-pulse correction during postflight data processing [as in Sadowy (1999)].

DUAL-FREQUENCY RATIO

Dual-frequency ratio (DFR) methods of analysis have demonstrated capabilities for inferring microphysical properties of hydrometeors, especially if one frequency is outside the Rayleigh regime (Liao et al. 2008). DFR is defined as the difference between radar reflectivity factor in two different frequencies, and can be expressed in the mathematical form: DFR $= 10 \log_{10} Z_1/Z_2$ where Z is in mm⁶ m⁻³, Z_1 is Ku band, and Z_2 is Ka band. In this way, if DFR is low (around 0 dB) in a particular area, the particles within that region are similar scatterers at both radar frequencies, typically within the Rayleigh scattering regime. If DFR is high, it often indicates that there is a departure from the Rayleigh scattering regime in one of the frequencies. High DFR can also be caused by attenuation differences between the two frequencies used. Liao and Meneghini (2011) demonstrated the potential for Ku- and Ka-band DFR to distinguish snow, mixed-phase, and liquid precipitation environments using both modeling and the Airborne Precipitation Radar (APR) Sadowy et al. (2003). DFR has also been used to infer the strength of deep convection cores, with high-DFR convective cores located in regions where greater updraft strength is expected (Ni et al. 2019).

Liao et al. (2016) found that snow density has the greatest effect on DFR-indicated volume-weighted mean diameter, suggesting that DFR can be used to infer qualities of precipitation beyond phase, precipitation intensity, and particle size. Chase et al. (2021) used GPM-frequency DFR products to conduct a quantitative retrieval of snow microphysical characteristics. A Ku- and Ka-band modeling study determined that single-crystal ice has a typical DFR around 0, while graupel ranges from 1.5 to 4, and snow aggregates range from 2.5 to 10 depending on the base ice crystal type (e.g., dendrites, needles, and rosettes) (Tyynelä and Chandrasekar 2014). Previous work has indicated that higher frequencies (such as the Ku, Ka, W, or G bands) tend to better characterize precipitation in DFR analyses; DFRs calculated with Ku and Ka bands have demonstrated promising results while largely avoiding attenuation issues that can impact other high-frequency bands more significantly (Tyynelä and Chandrasekar 2014).

3. Overview of methodology

Two days were chosen for analysis: 1 and 5 February 2020. On 1 February 2020, there was a radar bright band, indicative of the melting layer, that exhibited a distinct slanting behavior. The 5 February case featured a transition between rain and snow within flight legs. Since the 1 February flight occurred over ocean and the 5 February flight occurred over land, a comparison between the 2 days was also performed to investigate convective and stratiform clouds and precipitation features over both surface types. Two flight legs per day will be presented in this paper. These legs were chosen as they best exhibited the advantages and challenges of the different instruments for observing winter precipitation at high spatial and temporal resolution.

For this study, a radar bright band was defined as a vertically thin layer where at least a 12-dBZ difference was observed between the maximum reflectivity in the column and the vertical layer within 200 m of that maximum. This enhanced-reflectivity layer had to exist for the majority of a specific leg to be counted as a brightband leg. For 1 February, the vertical slopes (change in brightband altitude over time) of bright bands were estimated by drawing a straight line between the beginning and ending brightband altitudes along the leg. Least squares linear regressions were then performed with the estimated altitude and AMPR A-channel nadir brightness temperatures, which were calculated as the average of AMPR's two centermost pixels. The A channel was used due to its cleaner output relative to the B channel. Certain frequencies in the B channel exhibited prominent noise that could interfere with analysis.

In addition, AMPR's 85-GHz and CoSMIR's 89-GHz frequencies were highly correlated across days and various atmospheric and ground targets. Linear regression correlation analysis was performed between the T_b of these two frequencies for the full flight duration from both days. Coefficients of determination and mean offsets (where offset = AMPR − CoSMIR) were calculated for CoSMIR's along-track nadir pixel and the mean of AMPR's two centermost pixels for each entire flight, including takeoff, open land, rain, and snow. Across all possible permutations (e.g., 85A versus 89H and 85B versus 89V) and for

1 February, the coefficients of determination and offset averaged 0.98 and −1.7 K, respectively, while on 5 February the respective values were 0.98 and −0.6 K. This suggested good intercalibration of the instruments.

4. 1 February 2020

a. Overview

The research flight on 1 February took place during the deepening phase of a relatively warm cyclone over the western Atlantic. The two IMPACTS aircraft (ER-2 and P-3) sampled the cyclone and its associated frontal system before synching up with a GPM overpass (McMurdie et al. 2020, 2022). As shown in Fig. 1, there was a broad cloud deck. Within the top of the low cloud deck around 5-km altitude, cloud particles were composed largely of P-3 indicated supercooled liquid drops, while scattered within this cloud mass were narrow convective turrets above the bright band, sometimes in excess of 8 km above sea level, composed predominantly of ice (McMurdie et al. 2022). Below these cells was typically enhanced brightband reflectivity and inferred heavy precipitation reaching the surface. Both flight legs analyzed in this paper took place on the southern side of the comma-head cloud, but north of the surface low, observing both the broad cloud deck and convective turrets, which were diagnosed based on reflectivity structure.

b. Leg 1–1245 UTC

Figure 2 shows T_b swaths from both AMPR (left) and CoSMIR (right), with High-Resolution Rapid Refresh (HRRR) model analysis fields underlying the swath. The aircraft was moving from east to west during this leg, and the wind was largely easterly. The 850-hPa temperature and 500-hPa thickness both decreased to the north. Mean sea level pressure decreased to the east, toward the direction of the low.

The central pixels of AMPR's 10-GHz channel (Fig. 2a) were around 130 K at the beginning and end of the leg, which was within the range of possibly clear conditions or light rain. As the leg progressed westward, 10-GHz T_b began to increase, eventually reaching ~230 K near 35.4°N, 73°W. One would expect to find greater rain rates in those local T_b maxima (Spencer et al. 1994). Central pixel T_b then cooled and warmed intermittently, suggesting that a few distinct cells were generating higher precipitation rates than surrounding areas.

AMPR's 19-GHz (Fig. 2b) channel told a similar story. The lowest central pixel T_b was around 160 K at the beginning of the leg, which is consistent with ocean T_b (Spencer et al. 1994). The T_b value at this frequency began warming more readily than 10 GHz did and reached a maximum temperature of nearly 270 K inside the likely most heavily precipitating cell. The 19-GHz channel observed similar warming in precipitation around 35.7°N, 73.5°W.

The 37-GHz (Fig. 2c) channel began at a T_b of 190 K and reached a maximum temperature of 270 K much sooner than 19 GHz did. This was likely due to signal saturation, where the most heavily precipitating cells and the surrounding precipitation overwhelm contributions from the radiometrically cold ocean surface (Spencer et al. 1994). In the latter fourth
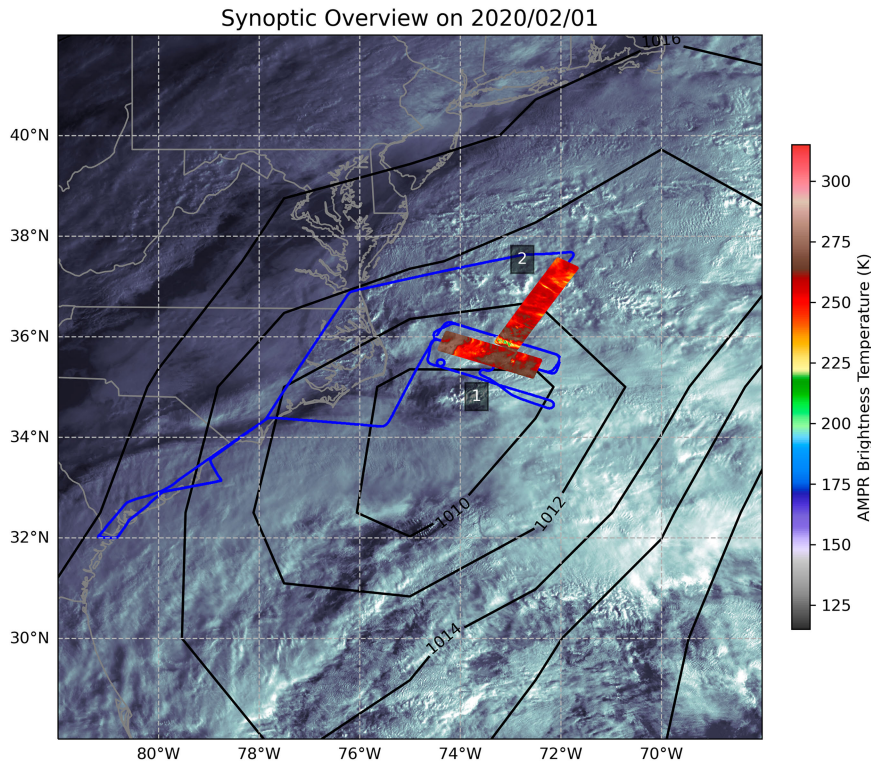
FIG. 1. Swaths of AMPR 85 GHz from each leg discussed on 1 Feb superimposed on the ER-2 full flight track (blue line), sea level pressure (black contours), and GOES visible imagery.

of the leg, there was a fluctuation in temperature between 74° and 74.5°W. Where the T_b rose to 240 K between two regions of cooler T_b (210–220 K), one would expect to find an isolated section of light precipitation, and there is radar evidence which will be discussed later

AMPR's 85-GHz channel (Fig. 2d) is more sensitive to cloud water and ice. Much of the leg appeared as an ambient T_b of 260–270 K, which is indicative of a liquid cloud deck (Spencer et al. 1994). Those locations where T_b decreased to 250 K or colder were more likely to be locations of ice scattering. One of the cells near 73.5°W reached a T_b maximum of 197 K in 10 GHz with a T_b delta of 63 between the cell and the surrounding environment, indicating the presence of liquid precipitation. It also caused a T_b minimum of 242 K in 85 GHz, indicative of ice scattering, with a T_b delta of 24 K. As will be shown later, this cell had taller cloud tops and likely a greater quantity of ice than the comparatively weaker emitters later in the leg.

All of CoSMIR's channels are sensitive to ice scattering. The swaths of both 89-GHz H and V (Figs. 2e,f, respectively) appear very similar to AMPR's 85-GHz swath, though there seemed to be some increased sensitivity to what were likely lower-altitude ice clouds in 89-GHz V, as there were a few more locations where the T_b dropped below 250 K. The highest two CoSMIR frequencies experienced greater cooling relative to the previous frequencies in response to the same targets. Of the four CoSMIR frequencies shown, 165 GHz appeared the most reactive to suspected ice presence, experiencing the greatest degree of T_b depression out of the ice-sensitive channels.

Figure 3 features nadir-view data from the three instruments. There was stratiform precipitation with embedded convective turrets, which is typical in the comma head. This structure, along with the prominent bright band, was nearly ubiquitous in the flight legs examined in this study. Reflectivity was weaker in the cloud mass above stratiform regions, relative to the deeper clouds over convective turrets.

Light stratiform rain (especially when less than 20 dBZ) demonstrated typical DFR values below 1.5 dB (Tyynelä and Chandrasekar 2014). Heavier rain featured higher DFR. For example, just before 1248 UTC, DFR increased in fallstreaks by about 3 dB just below the bright band. At 1249 UTC, DFR exceeded 17 dB in the core of a fallstreak.

In past studies, warm-cloud accretion processes have been found beneath comma head convective cells (Misumi et al. 2021), and particle growth can lead to hydrometeor sizes exceeding the Rayleigh scattering regime for Ka while remaining in the Rayleigh regime for Ku, increasing DFR. However, the effects of differential attenuation on Ku- and Ka-band data can be sizeable (Meneghini et al. 2015), and GPM Ku- and Ka-band DFR has been used to estimate differential path attenuation through rain? Meneghini et al. (2019).

While both attenuation and particle growth likely contributed to the observed DFR signature, attenuation is expected to have the greater impact here, especially as distance from the radar increases.

Interestingly, in the Ku-band reflectivity in Fig. 3a, the fallstreaks observed within 1254–1257 UTC below the bright
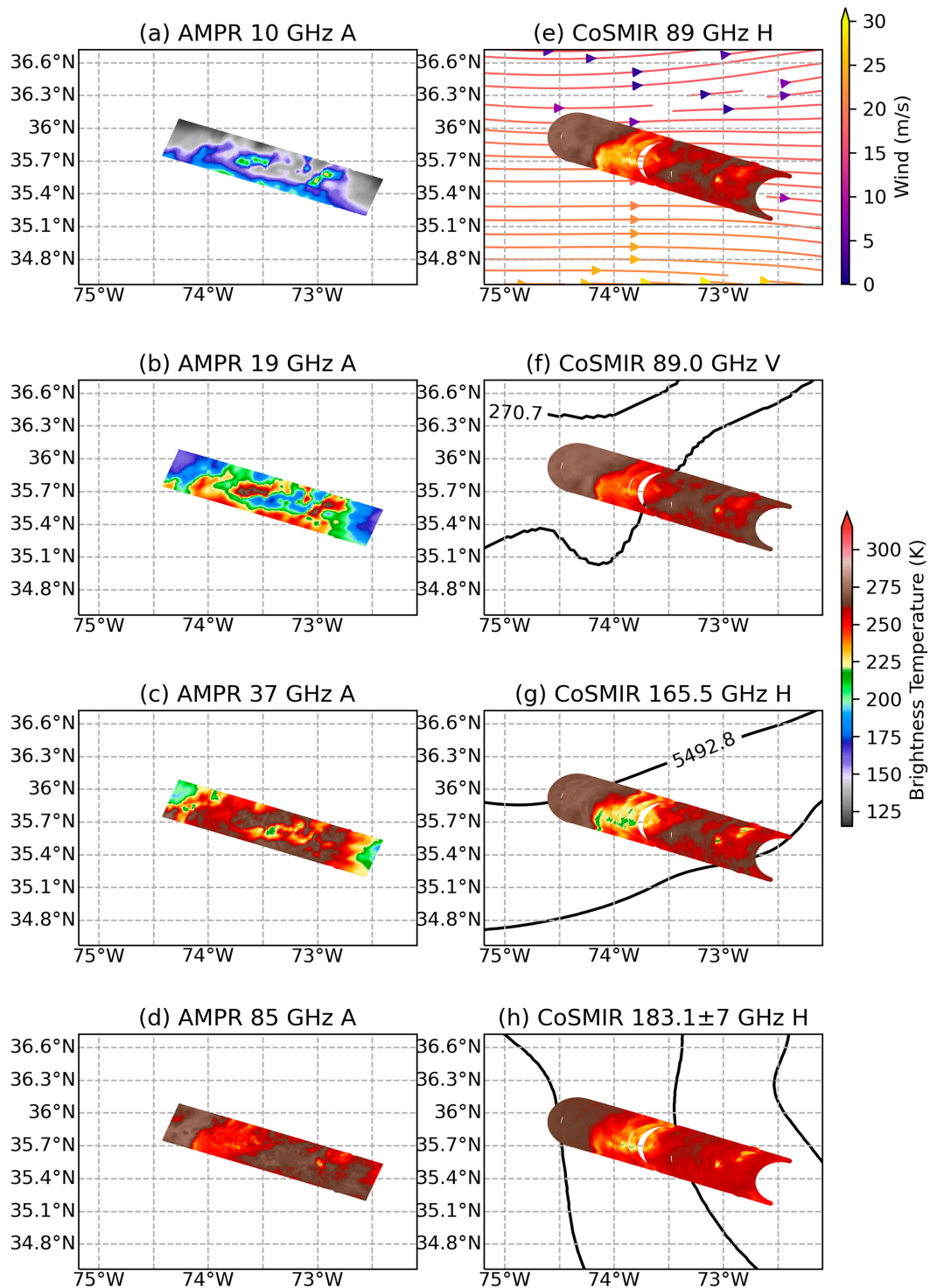
FIG. 2. Swaths of (left) AMPR and (right) COSMIR conical scan from 1245 to 1300 UTC. Channels included are AMPR (a) 10-GHz A, (b) 19-GHz A, (c) 37-GHz A, (d) 85-GHz A, and CoSMIR (e) 89-GHz H with wind streamlines, (f) 89-GHz V with 850-hPa temperature (K), (g) 165.5-GHz H with 500-hPa thickness, and (h) 183.1-GHz H with sea level pressure (hPa).
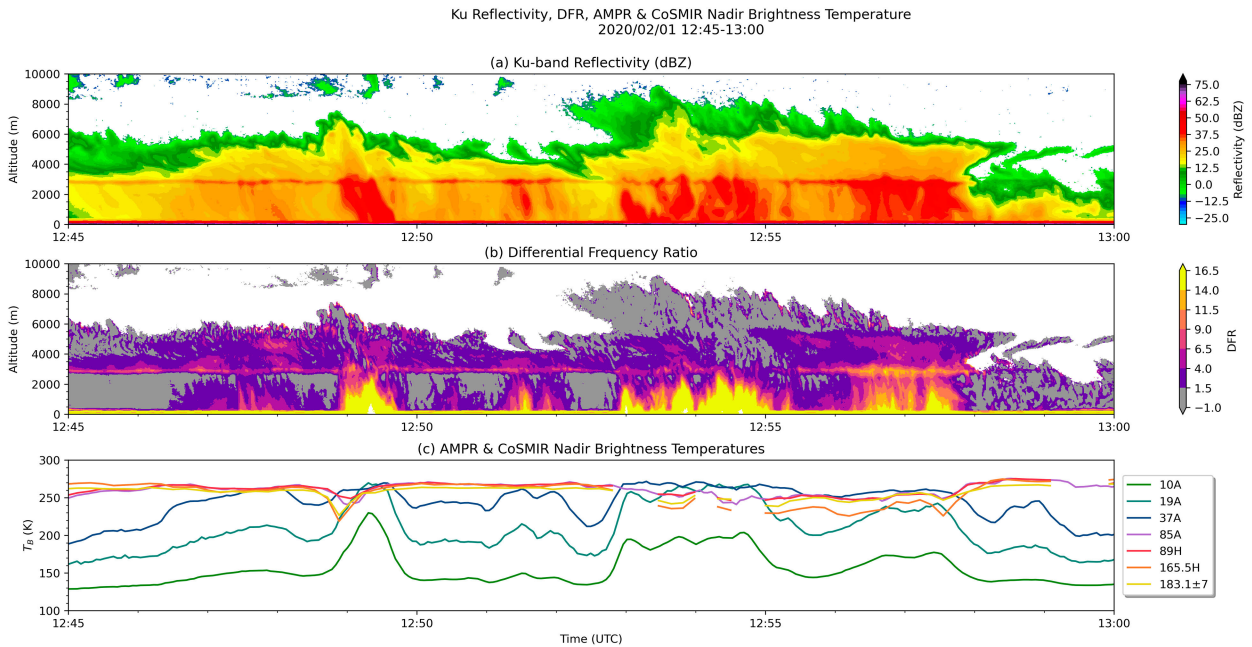
Ku Reflectivity, DFR, AMPR & CoSMIR Nadir Brightness Temperature
2020/02/01 12:45-13:00

FIG. 3. The 1245–1300 UTC 1 Feb HIWRAP (a) Ku-band reflectivity, (b) Ku–Ka DFR, and (c) nadir T_b from AMPR and CoSMIR. The Ku-band was generally more sensitive to precipitation and bright bands, so only Ku is pictured here. However, both frequencies are utilized in the DFR calculation.

band demonstrated similar reflectivity values (both reaching exceeding 40 dBZ). However, in the DFR curtain (Fig. 3b), the precipitation at 1254 UTC was associated with a low-DFR-value bright band (<10 dB) and high-value fallstreak DFR (>17 dB). The precipitation at 1257 UTC demonstrated a high-value brightband DFR (reaching 14 dB), with the fall-streak demonstrating overall lower DFR within the inferred heavy precipitation. There was a greater vertical extent of DFR exceeding 4 dB in the later precipitation, with a higher peak DFR above the bright band than was observed in the earlier region (in excess of 6 dB). The later precipitation fall-streaks were also associated with a bright band that exhibited both higher DFR (maximum DFR difference of 5 dB between the two bright bands).

The T_b indicated by the 10–37-GHz AMPR frequencies in Fig. 3c gradually grew warmer as Ku-band reflectivity indicated greater rates of liquid precipitation. Around 1248 UTC, a stark decrease in higher-frequency temperatures (from about 260 to 240 K for 85 and 89 GHz, and from 260 to 220 K for 165 and 189 GHz) is indicative of higher ice water content within the cloud mass, as radiation at those frequencies is scattered by ice particles, reducing the T_b observed by those radiometer channels (Hou et al. 2014; Spencer et al. 1994). An abrupt decrease in 85-, 89-, 165-, and 183 ± 7-GHz (hereafter referred to as 183) T_b could be observed at 1249 UTC. This was in association with an isolated cell where ascending motion aloft (inferred from HIWRAP Doppler velocity, not shown) could have led to the growth of ice-phase hydrometeors.

The response of the four higher frequencies to this cell featured substantial T_b deltas of 26 K for 85 GHz, 17 K for 89 GHz, 45 K for 165 GHz, and 33 K for 183 GHz. While retrievals of

particle types are outside of the scope of this study, the reflectivity structure at this time resembles that of graupel and aggregate-containing regions in Leinonen et al. (2018), and DFR in this location primarily falls into the ranges of graupel, dendrites, and aggregates of dendrites (1.5–7 dB), as found in Tyynelä and Chandrasekar (2014).

The latter half of this leg was characterized by intermittent heavy precipitation with ample cloud mass, followed by low radar reflectivity. The lower three AMPR frequencies (10–37 GHz) once again rose with increased precipitation intensity and declined in its absence. The 85- and 89-GHz channels cooled very similarly to each other throughout this portion of the flight. The 183-GHz channel featured intermittently stronger cooling than 85 or 89 GHz, possibly due to fluctuations in cloud ice or in relative humidity above the cloud Skofronick-Jackson and Johnson (2011). The 165-GHz frequency distinguished itself as featuring the coldest temperatures when observing precipitation scenes, particularly during the second half of the leg with more substantial reflectivity above the bright band.

During the last 2 min of the leg, HIWRAP-indicated reflectivity both above and below the brightband level are reduced in relation to the previous few minutes. The respective magnitude of the warming response from 1258 to 1259 UTC in the AMPR frequencies, particularly for 19 and 37 GHz (11 and 28 K, respectively), are in line with the sensitivity of each AMPR channel to cloud and liquid water outlined in Spencer et al. (1994).

c. Leg 2—1431 UTC

This leg began just to the north of the previous leg's northernmost edge (Fig. 1). It was oriented nearly perpendicular to

leg 1 and featured a greater number of isolated high-altitude cells, as opposed to the previous leg's broader cloud tops. In Fig. 4, which displays radiometer and HRRR data of the northernmost of the legs, 850-hPa temperature and 500-hPa height increased to the southeast. There was a component of wind crossing orthogonal to the flight path. At the southern end of the leg, localized warming signatures were seen in both 10 and 19 GHz (from 140 and 170 K up to approximately 250 and 270 K, respectively), indicating a band of strongly emitting liquid precipitation. North of this, there were two smaller clusters of similar-T_b precipitation. In this leg, the 37-GHz channel seemed to struggle in clearly resolving discrete features such as cloud pillars or fallstreaks compared to other frequencies, especially in the swath plot, though it does decrease throughout the leg (until 1445 UTC, which appeared to be 53 K cooler than the maximum T_b in 37 GHz for this leg) like the lower two frequencies.

The coldest locations in 37 GHz (<240 K) largely appeared to be caused by either reduced liquid precipitation relative to the surrounding area (as judged by lack of substantial warming signatures in those locations in 10 and 19 GHz), increased ice particle mass relative to the surrounding area (indicated by $T_b < 265$ K in 85-GHz and higher frequencies), or a combination thereof. A broad cloud deck was observable in all CoSMIR swaths, with a banding structure visible as localized T_b minima (often <250 K, but capable of reaching below 220 K). This expression of banding in CoSMIR swaths was most prominent in 165 and 183 GHz. The coldest T_b in the leg was nearly 190 K in the 165-GHz frequency.

The curtain view provided in Fig. 5 showed trends similar to the previous leg with respect to different precipitation environments. Brightband DFR in Fig. 5b ranged between 4 and 17 dB or greater. Fallstreaks of various reflectivities in Fig. 5a (between 35 and 50 dBZ) generally demonstrated increasing DFR approaching the ground. Raindrop growth through collision–coalescence could contribute to DFR increases below the bright band, but again, differential attenuation is expected to be greatly impactful on the DFR of these fallstreaks.

The 10-GHz AMPR channel in Fig. 5c responded less to precipitation than 19 or 37 GHz. It did resolve the precipitation at 1432 UTC, which appeared to attenuate the Ku-band signal below 2 km and whose maximum fallstreak reflectivity exceeded 47 dBZ. The 19-GHz channel resolved areas of likely lighter precipitation with more detail, but was prone to saturation in heavier precipitation (e.g., around 1432 UTC). Largely saturated for the first half of the leg, 37 GHz only demonstrated a notable decline in T_b once the precipitation rate eased after 1442 UTC.

As was shown in frequencies higher than 37 GHz (Fig. 4), the cloud deck was quite broad and varied in this leg. There were five rather distinct local T_b minima observable in Fig. 5 in 183 GHz at 1432, 1436, 1438, 1440, and 1443 UTC. There were further T_b depressions at 1435 UTC in 165 GHz especially, and a broad fluctuating scattering signature at and after 1445 UTC. The CoSMIR-frequency T_b observed here are within the range of those observed over water for snow and convection events (Panegrossi et al. 2017; Katsumata et al. 2000). In Spencer et al. (1994), comparable 85-GHz T_b were observed in anvil material that had advected away from the main core of thunderstorms over a water surface.

Each of the five main instances of ice scattering observed in Fig. 5c were associated with high-altitude cloud tops with reflectivities exceeding 15 dBZ. The 15-dBZ echo-top heights, as well as the minimum brightness temperatures of the four highest radiometer frequencies (85–183 GHz), are logged in Table 1. The coldest T_b and strongest scattering were associated with the second-highest cloud plume of the group at 1432 UTC (up to 8.3 km), which was directly above precipitation early in the leg. The highest cloud plume at 1443 UTC (8.7 km high) featured the second-lowest T_b, at an average of 11 K warmer than the coldest cloud. Here 165 GHz displayed the greatest change and 183 GHz experienced the least. While higher cloud tops typically resulted in lower 85–183-GHz brightness temperatures, there were exceptions. The cloud mass at 1432 UTC was significant enough to result in colder T_b than that which was observed in association with the tallest cloud top. Similarly, the two 7.9-km clouds at 1436 and 1438 UTC appeared colder than the cloud at 1440 UTC, which was taller.

Additionally, there was a distinct downward slope in brightband altitude throughout the duration of the leg, observable in Fig. 5a. There was a coincident downward slope in the recorded T_b in AMPR frequencies as well (Fig. 5c), and two other legs demonstrated similar relationships between brightband altitude and AMPR brightness temperatures. Thus, a correlation analysis was done for these three legs. Table 2 details the time at the start of an uninterrupted bright band, its duration (length of time that the bright band remains visible in the Ku-band curtain, effectively a distance), the beginning and ending altitudes of the bright band (altitude of the approximate center of the bright band at the time when it becomes visible/stops being visible), and the coefficients of determination for each segment using each frequency. Brightband identification was conducted manually, prioritizing areas where the bright band (American Meteorological Society 2022; Pfaff et al. 2014), was largely continuous for several minutes of flight time.

The durations and brightband altitude changes of the 1245 and 1307 UTC legs (Note: The 1307 UTC leg was not analyzed in detail in this paper.) were similar. Both legs were least correlated at 10 GHz, and most correlated at 37 GHz. The 1433 UTC leg had the longest and most intensely sloped bright band of the day. It descended roughly 700 m while the others only descended by around 200 m. The 1433 UTC leg also demonstrated the highest correlation between brightband slope and AMPR T_b slope.

Though each bright band descended, the earliest two bright bands were associated with overall greater variability in reflectivity and DFR near the surface (e.g., Fig. 3). The earlier legs with lower correlation also only had just 200 m of brightband altitude change. Meanwhile, the 1433 UTC leg was oriented more orthogonal to the thermal gradient (e.g., Fig. 4). Further investigation could include accounting for finer fluctuations in brightband altitude, as well as for precipitation rate, cloud-top altitude, cloud liquid water path, and other attributes.
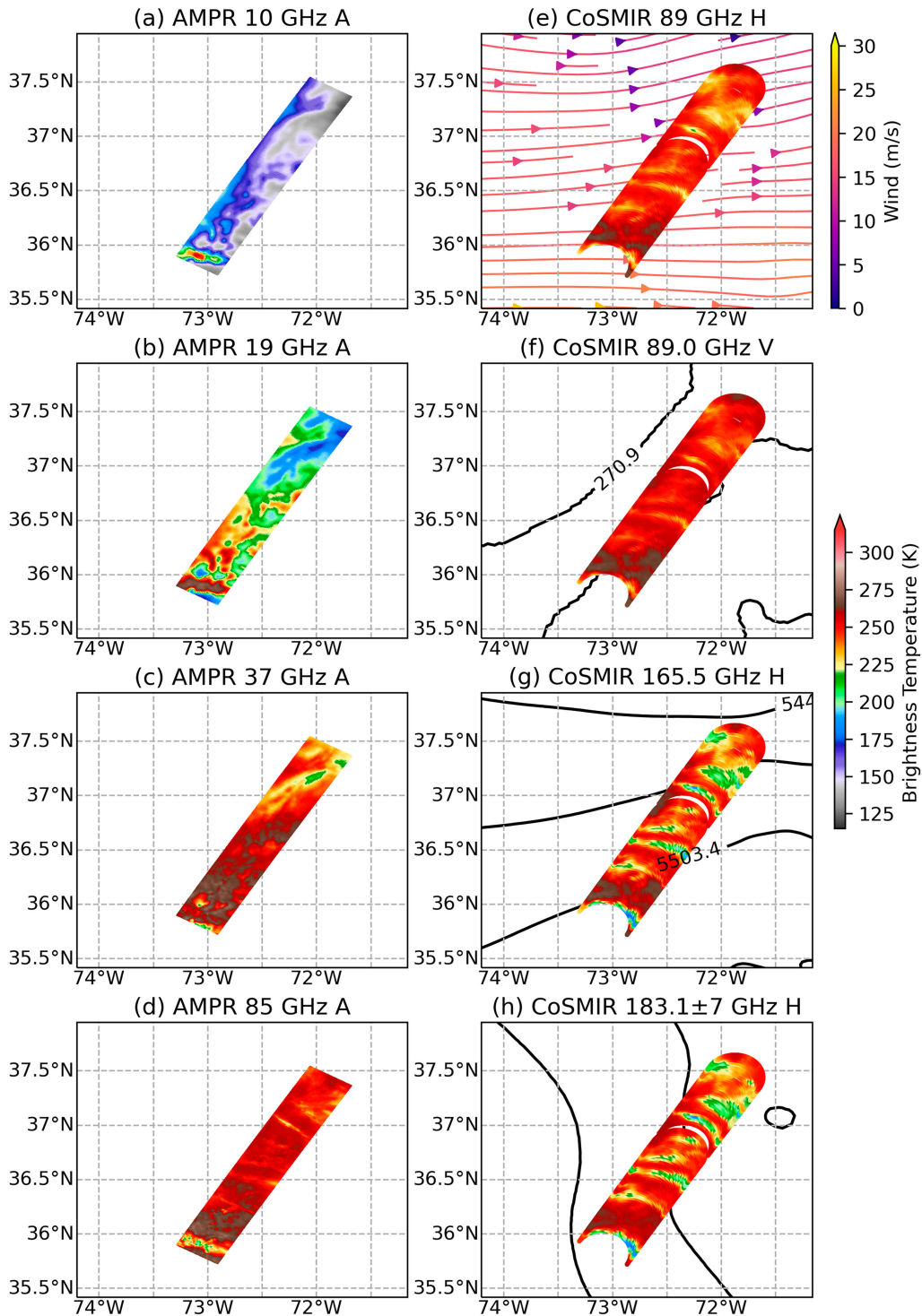
FIG. 4. Swaths of (left) AMPR and (right) CoSMIR conical scan from 1431 to 1448 UTC. Channels included are AMPR (a) 10-GHz A, (b) 19-GHz A, (c) 37-GHz A, (d) 85-GHz A, and CoSMIR (e) 89-GHz H with wind streamlines, (f) 89-GHz V with 850-hPa temperature (K), (g) 165.5-GHz H with 500-hPa thickness, and (h) 183.1-GHz H with sea level pressure (hPa).
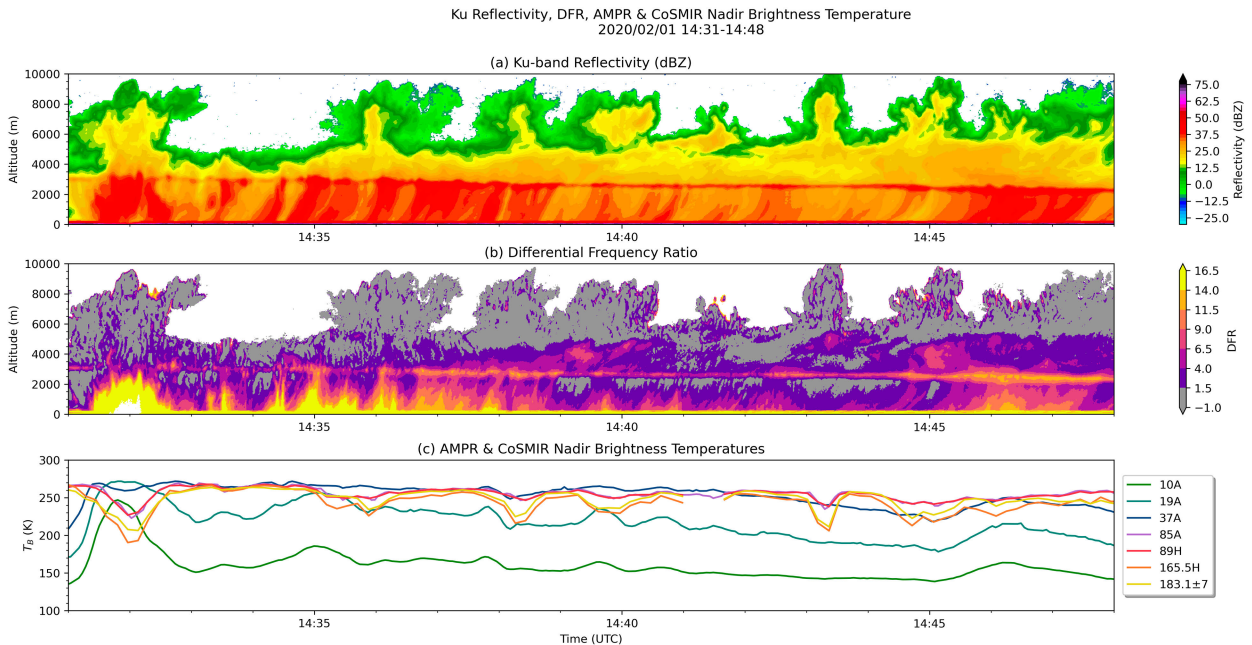
FIG. 5. The 1431–1448 UTC 1 Feb HIWRAP (a) Ku-band reflectivity, (b) Ku–Ka DFR, and (c) nadir T_b from AMPR and CoSMIR. The Ku-band was generally more sensitive to precipitation and bright bands, so only Ku is pictured here. However, both frequencies are utilized in the DFR calculation.

5. 5 February 2020

a. Overview

The flight on 5 February occurred over the comma head of a developing cyclone, the center of which was over the lower Mississippi Valley (Fig. 6). An elevated warm front was observed oriented northeast–southwest, overrunning preexisting cold air over Missouri, Illinois, and Indiana (Finlon et al. 2022). The flight sampled dry, snow-covered, and wet land, as well as rivers, liquid and ice precipitation, and even some urban landscape. The liquid precipitation was structurally similar to that which was seen on 1 February (light precipitation with embedded higher-reflectivity cells). Some of the ice precipitation was organized into bands (McMurdie et al. 2022).

b. Leg 1—2055 UTC

In Fig. 7, the flight leg progressed from southeast to northwest with temperature and height decreasing and pressure increasing along the leg. There was a 750-hPa southwesterly crosswind that weakened to the north. Multiple rivers were

observed in AMPR's frequencies and in the vertically polarized 89-GHz data from CoSMIR (Fig. 7). The 10-GHz frequency demonstrated cooling signatures in the first third of the flight leg, to below 180 K, in association with ground wetting from rain. This cooling signature weakened as frequency increased, to 230 K at 19 GHz and 240 K at 37 GHz, while at 85-GHz and higher frequencies the surface emission gave way to a cloud-based ice scattering signal. Further north, the lower frequencies returned to T_b resembling unobstructed dry land radiance. The CoSMIR frequencies, however, continued seeing colder T_b throughout the leg, suggesting the presence of ice clouds.

In Fig. 8, the leg began with a small convective turret leading into a descending bright band as the aircraft traveled northwest across the front. The skin paint of the P-3 aircraft is visible at 2117 UTC at 5 km as a high-reflectivity, high-DFR object. Within the liquid precipitation regime (prior to 2110 UTC), there existed a similar high-frequency (85+ GHz) passive microwave response to convective turrets as was observed on 1 February. For the 6–8-km cells at 2056, 2100, and 2102 UTC,

TABLE 1. Approximate time of cloud pass-over, maximum height of that cloud's 15+ dBZ echo, and the recorded T_b of the four highest frequencies used in this analysis (AMPR's 85-GHz and CoSMIR's 89-, 165-, and 183-GHz frequencies) in association with the cloud.

Time (UTC)	Max height (km)	85 GHz (K)	89 GHz (K)	165 GHz (K)	183 GHZ (K)
1432	8.3	224	227	191	207
1436	7.9	247	249	226	235
1438	7.9	247	247	216	226
1440	8.1	250	250	230	236
1443	8.7	235	239	207	212

TABLE 2. The first four columns show the start time, duration, start altitude, and end altitude of sloped bright bands on 1 Feb 2020. These were the values used to estimate bright band slope. The last four columns show coefficients of determination for AMPR nadir T_b and brightband altitude.

Start time (UTC)	Duration (min)	Start height (km)	End height (km)	AMPR frequency and R^2 value			
				10 GHz	19 GHz	37 GHz	85 GHz
1245	12	2.92	2.72	0.17	0.30	0.33	0.22
1307	13	2.90	2.70	0.031	0.089	0.13	0.042
1433	15	2.93	2.24	0.43	0.65	0.70	0.32

all 85–183-GHz channels showed substantial cooling, especially for the 2102 UTC cell where 85 and 89 GHz decreased by ~20 K, 165 GHz by ~60 K, and 183 GHz by ~40 K. The lower radiometer frequencies demonstrated cooling in response to the broader liquid precipitation area (by nearly 20 K for 10 GHz and 19 GHz, and 5 K for 37 GHz), with localized warming signatures in response to increased rain intensity (i.e., up to 230 K in 10 GHz, 240 K in 19 GHz, and 255 K in 37 GHz between 2100 and 2102 UTC). As rain began to transition to snow after 2105 UTC, these lower three frequencies increased in temperature to 260 K by 2115 UTC. Finer observation of this transition in radiometer data was unfortunately interrupted by passage over a river at 2107 UTC.

This interruption has important implications for the use of radiometer data over land. If a surface feature is sizeable or radiatively strong enough, it will overwhelm the signal from meteorological features. In a modeling study that assessed scene contributions to radiometer T_b, hydrometeors were found responsible about 25% and 30% of T_b values for the 166-GHz and 183 ± 7-GHz frequencies, respectively, with the respective majority of T_b being determined by surface emission and relative humidity during a WRF-simulated synoptic snow case (Skofronick-Jackson and Johnson 2011). In lower-frequency channels, more than 65% of T_b contribution was from surface emission.

The transition in surface precipitation phase (rain-snow transition) featured all frequencies increasing in T_b during 2106–2112 UTC. After 2108 UTC, the degree of change in radiometer-indicated T_b (slope) became less severe until there was only apparent snow visible in the radar by 2112 UTC. During this time frame, 10 GHz experienced the greatest T_b increase (~20 K). The 183-GHz channel experienced the least net increase (~1 K). The frequencies ≥ 85 GHz cooled somewhat across the transition, and multiple frequencies experienced a brief dip in T_b at 2109 UTC before increasing slightly. Though this occurs in conjunction with the transition, these
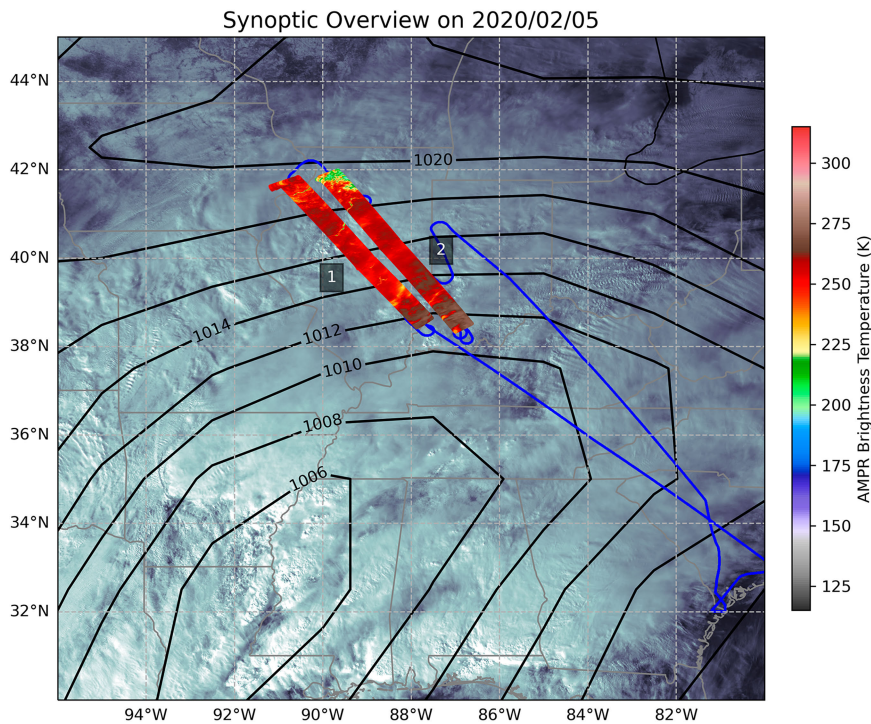

FIG. 6. Swaths of AMPR 85 GHz from each leg discussed on 5 Feb superimposed on the ER-2 full flight track (blue line), sea level pressure (black contours), and GOES visible imagery.
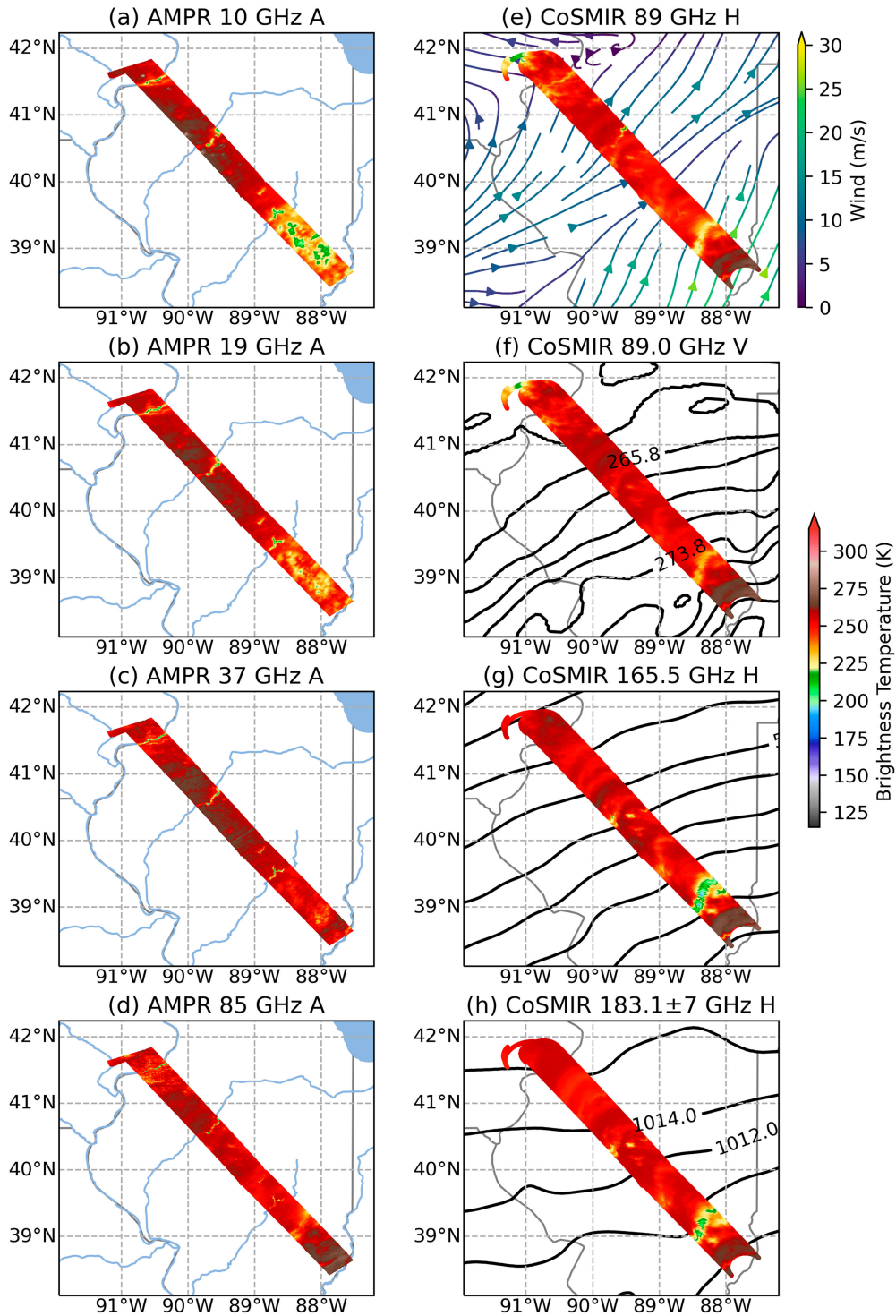
FIG. 7. Swaths of (left) AMPR and (right) CoSMIR conical scan from 2055 to 2132 UTC. Channels included are AMPR (a) 10-GHz A, (b) 19-GHz A, (c) 37-GHz A, (d) 85-GHz A, and CoSMIR (e) 89-GHz H with wind streamlines, (f) 89-GHz V with 850-hPa temperature (K), (g) 165.5-GHz H with 500-hPa thickness, and (h) 183.1-GHz H with sea level pressure (hPa).
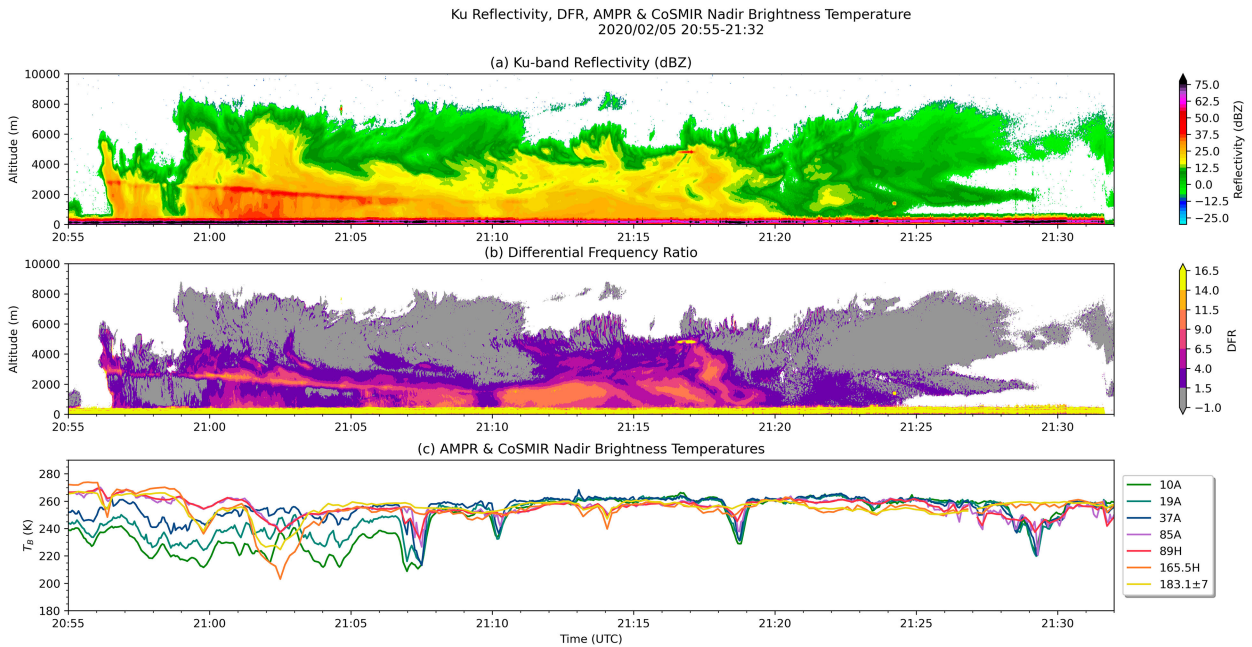
Ku Reflectivity, DFR, AMPR & CoSMIR Nadir Brightness Temperature
2020/02/05 20:55-21:32

FIG. 8. The 2055–2132 UTC 5 Feb HIWRAP (a) Ku-band reflectivity, (b) Ku–Ka DFR, and (c) nadir T_b from AMPR and CoSMIR. The Ku-band was generally more sensitive to precipitation and bright bands, so only Ku is pictured here. However, both frequencies are utilized in the DFR calculation.

high-frequency T_b changes could also be caused by changes within the clouds. There was no obvious single feature in reflectivity or DFR that would easily explain this. There did exist a cloud pillar of about 16 dBZ at 3.5 km. As there was still a semblance of bright band beneath this, perhaps cloud ice particles were creating cooling in the high frequencies, and a small amount of liquid precipitation was creating low-frequency cooling by wetting the ground. It is also possible that a small landbased feature was responsible for this.

There did appear to be a few high-frequency T_b depressions after the transition in the snow region, which were unrelated to apparent surface features like rivers, such as the cooling signatures at 2114, 2118, and 2122 UTC. These appeared as relative T_b depressions of 2–5 K. The 165- and 183-GHz frequencies tended to cool more readily than 85 and 89 GHz. These T_b depressions appeared to correspond with convective turrets (particularly at 2114 UTC). However, there was a much broader enhancement in radar reflectivity and DFR during 2110–2118 UTC that was likely associated with snow, so the higher-frequency radiometric response was mostly related to enhanced vertical development and higher-altitude clouds, rather than obvious enhancements in precipitation at the surface.

c. Leg 2—2141 UTC

This leg was a return flight, occurring just after and to the east of the previous leg (Fig. 6). Mesoscale conditions shown in Fig. 9 were largely similar as well, but now the aircraft was crossing the front southward toward the warm sector. There was cooling in all radiometric channels at the northwestern tip of the leg, which will be investigated later. Then the Illinois

River was apparent in all AMPR channels and CoSMIR's 89-GHz channels, especially 89-GHz H. After that, warmer temperatures associated with dry (or snow-covered) ground were observed at 10–37 GHz, before giving way to cooling toward the south, likely associated with ground wetting from the rain in the warm sector. In addition to this, periodically along the leg there was intermittent cooling in frequencies ≥ 85 GHz that was likely indicative of ice scattering. A substantial cold signature at 165 GHz appeared at the very end of the leg in Fig. 9g. Unfortunately, the aircraft began a turn immediately after this, so further analysis of that signature was not possible.

Figure 10 shows the corresponding curtain plot for this leg. As in the previous leg (Fig. 8), the snow-rain transition (after 2200 UTC) involved a ~20-K T_b change at 10 GHz, with similar but less pronounced responses from 19 to 37 GHz. Frequencies ≥ 85 GHz did not respond substantially to the land surface moistening after 2200 UTC. However, they did respond to the presence of various convective turrets after 2200 UTC, particularly around 2209 and 2213 UTC.

Within the snow portion of this leg (i.e., before 2200 UTC), there was a high-frequency (85+ GHz) T_b decrease around 2151 UTC. It was associated with a radar-detected echo top more than 1 km taller than the surroundings. However, around 2155 UTC there was a similar increase in echo-top height, with an even greater enhancement in low-level DFR compared to 2151 UTC, but there was no significant deviation in radiometer T_b.

Finlon et al. (2022) demonstrated that variability in cloud microphysical properties could appear as regions of different DFR, and Skofronick-Jackson et al. (2013) determined that
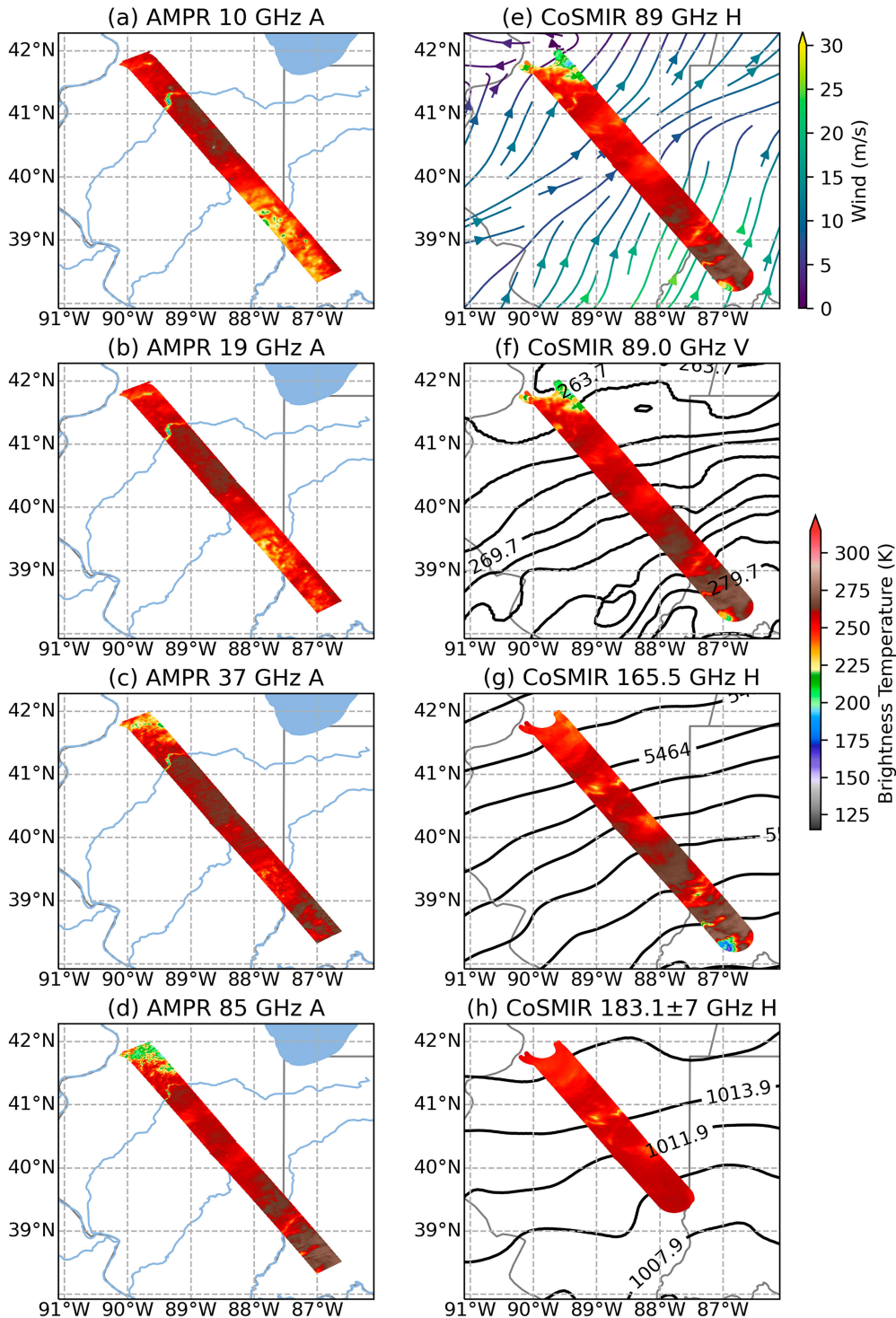
FIG. 9. Swaths of (left) AMPR and (right) CoSMIR conical scan from 2141 to 2216 UTC. Channels included are AMPR (a) 10-GHz A, (b) 19-GHz A, (c) 37-GHz A, (d) 85-GHz A, and CoSMIR (e) 89-GHz H with wind streamlines, (f) 89-GHz V with 850-hPa temperature (K), (g) 165.5-GHz H with 500-hPa thickness, and (h) 183.1-GHz H with sea level pressure (hPa). CoSMIR 183-GHz swath has been truncated due to missing data.
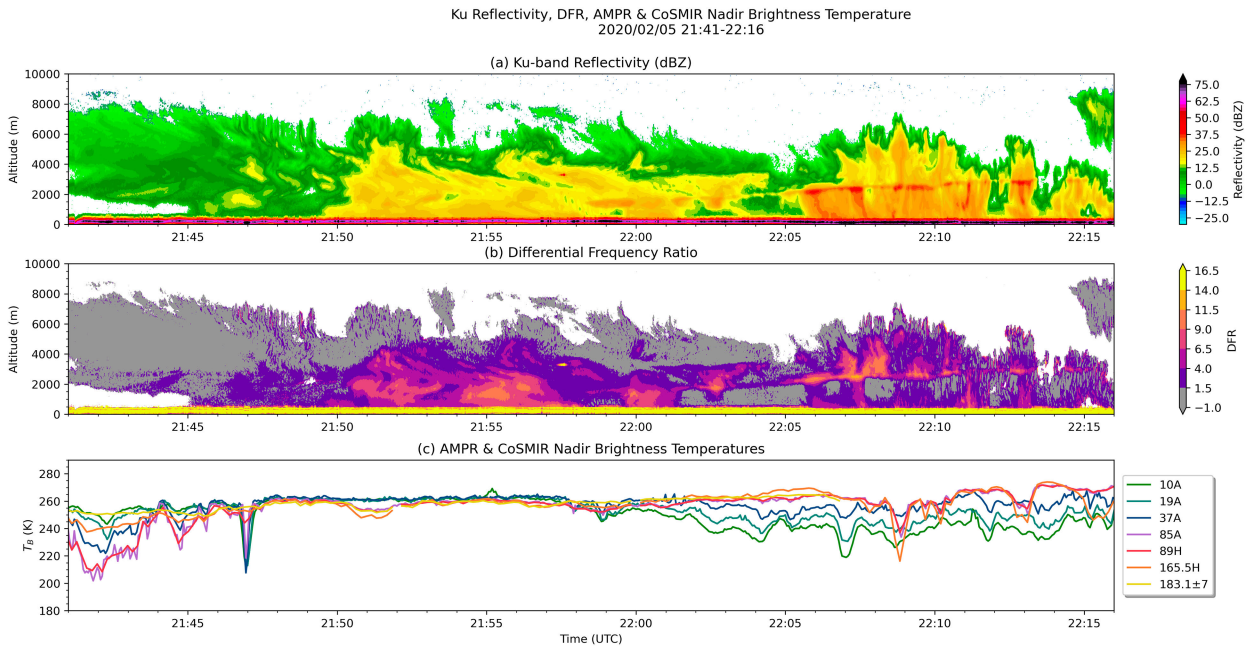
Ku Reflectivity, DFR, AMPR & CoSMIR Nadir Brightness Temperature
2020/02/05 21:41-22:16

FIG. 10. The 2141–2216 UTC 5 Feb HIWRAP (a) Ku-band reflectivity, (b) Ku–Ka DFR, and (c) nadir T_b from AMPR and CoSMIR. The Ku-band was generally more sensitive to precipitation and bright bands, so only Ku is pictured here. However, both frequencies are utilized in the DFR calculation.

cloud structure and microphysics have a substantial impact on the ability of instruments to detect meteorological targets. It is not unreasonable, then, to postulate that these differences in radiometer behavior were influenced by microphysical or structural differences between clouds.

6. Conclusions

a. Radiometers

Overall, radiometers demonstrated proficiency in identifying many different degrees of precipitation and ice mass in an atmospheric column when over water. The best channels for detecting the presence of light precipitation over water were 19 and 37 GHz. The 37-GHz frequency saturated the most quickly, reaching 262 K at 1248 UTC 1 February (near the maximum observed T_b for 37 GHz of 271 K within the 1 February legs) even when Ku-reflectivity throughout the column at that time did not exceed 30 dBZ. Because of this tendency, the inclusion of 19 and 10 GHz was important to resolve inferred moderate-to-heavy liquid precipitation. In perhaps the most intense precipitation on 1 February, at 1432 UTC, even 19 GHz appeared to have saturated, leaving 10 GHz to resolve the convective turret as the warmest meteorological target analyzed across the two flight days. Thus, AMPR's lowest radiometer frequencies together provided valuable information regarding precipitation location and intensity.

The 85-GHz (AMPR) and 89-GHz (CoSMIR) nadir T_b were very well correlated despite instrument differences (e.g., polarization, resolution, frequency) over a multitude of surface types and meteorological targets. The behavior of the two

channels during 1 February's first leg also indicated that they were sensitive to liquid hydrometeors, as they warmed in response to quite sparse liquid presence. However, their sensitivity to cloud ice caused them to cool in instances like convective turrets on both case days. CoSMIR's 165- and 183-GHz frequencies did not warm in response to liquid like 85 and 89 GHz. Rather, they experienced greater cooling in response to cloud ice, exemplified well during 1 February's second leg. The response to cloud microphysical changes was stronger at 165 GHz versus 183 GHz. Overall, The differential response in all frequencies used in this analysis emphasize the importance of multichannel analysis of radiometer products.

There also was some correlation between AMPR T_b and brightband altitude when flying over an ocean surface. This relationship was strongest for the leg with the most dynamic change in brightband altitude. Though there are many confounding factors (e.g., variability in precipitation rate), a higher-altitude bright band would in general allow for more cumulative liquid mass in the column below it, resulting in greater emission and higher T_b.

Over land, radiometric analysis was complicated by variability in land surface type and soil moisture. The liquid-sensitive frequencies (i.e., 10, 19, and 37 GHz) responded strongly to surface emissivity, making it difficult to decipher meteorological signals if radiometer data were used without supplementary radar. At higher frequencies (85+ GHz), ice scattering signatures seemed to correspond best with the presence of higher-altitude convective turrets, rather than significant changes in near-surface precipitation (at least as indicated by HIWRAP reflectivity and DFR). Radiometer use over land is best accompanied by surface emissivity data or other supplementary products to derive

the greatest degree of information, particularly when dealing with wintertime precipitation.

b. Radar products

In Liao and Meneghini (2011), mixed-phase precipitation was distinct as having, on average, the highest Ku-band reflectivities as well as the highest DFR values of any precipitation phase category in stratiform storms. Imagery from 5 February are in agreement with those results. Values of DFR within the bright band could exceed 15 dB, making mixed-phase regions among the brightest targets within the DFR field. Above the bright band, DFR was generally lower in low-reflectivity clouds or the higher-altitude edges of clouds visible in Ku-band reflectivity. When convective turrets were present, DFR exceeding 5 dB often extended upward from the bright band. This could be due to a combination of convection mixing precipitation phases and enhanced ice growth and aggregation within the convective turrets.

DFR generally ranged between 1 and 2 dB in light rain. However, in heavier rain, DFR could increase in excess of 16 dB. In the case of snow, moderate DFR values (around 10 dB) seemed to correspond with areas where substantial snow aggregation could be expected (i.e., just above the melting layer, where aggregation is most efficient) (Griffin et al. 2020; McFarquhar et al. 2007). If future work is done to thoroughly characterize DFR in various crystal habits, it could become a powerful tool in a radar analyst's toolkit to assess possible snow precipitation rates with relatively high temporal resolution.

DFR could also be used to investigate differences in microphysical properties between similar precipitation features. For instance, even when bright bands and rain intensity appeared similar in Ku imagery, those features could have very different DFR values. This was exemplified in Figs. 5 and 8. In Fig. 5 between 1440 and 1445 UTC, a clear bright band existed above light to moderate rain. A similar situation existed in Fig. 8 between 2100 and 2105 UTC. Looking at the surface level, these two legs even demonstrated similar DFR at the ground, generally hovering around values of 5–7 dB. However, the brightband DFR of these two legs were distinct from one another. The DFR of the 1 February leg mostly peaked around 7 dB, while the 5 February leg often exceeded 11 dB. The type and shape of melting particles in the bright band likely caused these differences.

In future studies, data produced by instrumentation aboard the P-3 aircraft could be utilized. The P-3 also flew with the IMPACTS field campaign, and is a cloud-penetrating aircraft. Instruments aboard the P-3 included a precipitation probe, in situ atmospheric monitoring, and the release of dropsondes. The data from these instruments could facilitate analysis of snow crystal effective density, liquid water content, crystal habit, and other bulk properties associated with the hydrometeor population within the storms. A study utilizing both DFR and particle size distribution measurements was conducted by Finlon et al. (2022), with the intent to improve the representation of precipitation in forecasting models and satellite retrievals. Further work on this topic could serve as further validation and refinement of DFR analysis, which could then be applied to GPM DPR data.

c. Combined utility

Radar revealed microphysical variations within a column better than the radiometers, which especially over land were most sensitive to either higher-altitude clouds or surface emission. As a result of their inherent integrative properties, however, the radiometers were well equipped to assess bulk hydrometeor mass in a column, depending on surface type and frequency. Use of multiple radiometer frequencies in aggregate also could be used to infer meteorological variations within a column's depth over multiple surface types, as was demonstrated in Spencer et al. (1994). Radar and radiometer both were able to convey information regarding cloud-top height over water, as was observed on 1 February, when radar-indicated cloud tops appeared to correlate with T_b depressions at 85+ GHz. Over water, both radar and radiometers could readily identify localized maxima in precipitation rate in convective turrets.

Over land, most meteorological targets were better detected with radar. Radar interpretation was unperturbed by the complexities of land surface emission, and could identify clouds, liquid precipitation of many intensities, and snow just as well over land as over water. Meanwhile, distinguishing dry land from surface snow was quite difficult with radiometer data alone, and when meteorological targets were observed above dry or snowy land, it was likewise difficult to identify those phenomena without the presence of ice scattering, which as mentioned above seemed to correspond more strongly with echo-top height than actual precipitation rate. When over wet land, many radiometer frequencies (particularly 10–89 GHz) demonstrated greater responses to meteorological targets, akin to what was observed over water.

Regarding the detection of meteorological features using these instruments versus the lower-resolution GPM sensors, GPM would likely be able to detect the presence of and locations of precipitation and cloud ice, at least in radar. The narrowest cloud pillars in Fig. 5 were around 2–3 km wide. These narrowest turrets could be difficult to detect by DPR and GMI, and in GMI especially there would be difficulty in determining the horizontal extent of the cloud pillar, as the finest ground resolution in GMI's frequencies is 4.4 km × 7.3 km (Hou et al. 2014). It appears that DPR did resolve the sloping bright band on 1 February (McMurdie et al. 2022), though much more coarsely than the airborne radars. DPR likely would struggle with fully resolving the rapid changes in DFR around and within the bright bands observed throughout the legs discussed in this study. These results demonstrate the continued value of suborbital measurements for studying cloud microphysical process at high resolution.

Brian_Blaylock (doi: http://doi.org/10.7278/S5JQ0Z5B). NCEP reanalysis and *GOES-16* data for Figs. 1 and 6 can be obtained from https://psl.noaa.gov/data/reanalysis/reanalysis.shtml and https://www.avl.class.noaa.gov/saa/products/welcome, respectively. IMPACTS data are archived at the NASA Global Hydrometeorology Resource Center DAAC McMurdie et al. (2019; doi: http://doi.org/10.5067/IMPACTS/DATA101). This includes datasets from AMPR (doi: http://doi.org/10.5067/IMPACTS/AMPR/DATA101), CoSMIR (doi: http://doi.org/10.5067/IMPACTS/COSMIR/DATA101), and HIWRAP (doi: http://doi.org/10.5067/IMPACTS/HIWRAP/DATA101).

REFERENCES

American Meteorological Society, 2022: Bright band. Glossary of Meteorology, https://glossary.ametsoc.org/wiki/Bright_band.

Amiot, C. G., S. K. Biswas, T. J. Lang, and D. I. Duncan, 2021: Dual-polarization deconvolution and geophysical retrievals from the advanced microwave precipitation radiometer during OLYMPEX/RADEX. *J. Atmos. Oceanic Technol.*, **38**, 607–628, https://doi.org/10.1175/JTECH-D-19-0218.1.

Blaylock, B. K., J. D. Horel, and S. Liston, 2017: Cloud archiving and data mining of high resolution rapid refresh model output. *Comput. Geosci.*, **109**, 43–50, https://doi.org/10.1016/j.cageo.2017.08.005.

Carlin, J. T., and A. V. Rhyzkov, 2019: Estimation of melting-layer cooling rate from dual-polarization radar: Spectral bin model simulations. *J. Appl. Meteor. Climatol.*, **58**, 1485–1508, https://doi.org/10.1175/JAMC-D-18-0343.1.

Chase, R. J., S. W. Nesbitt, and G. M. McFarquhar, 2021: A dual-frequency radar retrieval of two parameters of the snowfall particle size distribution using a neural network. *J. Appl. Meteor. Climatol.*, **60**, 341–359, https://doi.org/10.1175/JAMC-D-20-0177.1.

Doviak, R. J., and D. S. Zrnic, 1993: *Doppler Radar and Weather Observations.* Academic Press, 562 pp.

Draper, D. W., D. A. Newell, F. J. Wentz, S. Krimchansky, and G. M. Skofronick-Jackson, 2015: The Global Precipitation Measurement (GPM) microwave imager (GMI): Instrument overview and early on-orbit performance. *IEEE J. Sel. Top. Appl. Earth Obs. Remote Sens.*, **8**, 3452–3462, https://doi.org/10.1109/JSTARS.2015.2403303.

Finlon, J. A., L. A. McMurdie, and R. J. Chase, 2022: Investigation of microphysical properties within regions of enhanced dual-frequency ratio during the impacts field campaign. *J. Atmos. Sci.*, **79**, 2773–2795, https://doi.org/10.1175/JAS-D-21-0311.1.

Griffin, E. M., T. J. Schuur, and A. V. Rhyzkov, 2020: A polarimetric radar analysis of ice microphysical processes in melting layers of winter storms using S-band quasi-vertical profiles. *J. Appl. Meteor. Climatol.*, **59**, 751–767, https://doi.org/10.1175/JAMC-D-19-0128.1.

Herzegh, P. H., and P. V. Hobbs, 1980: The mesoscale and microscale structure and organization of clouds and precipitation in midlatitude cyclones. II: Warm-frontal clouds. *J. Atmos. Sci.*, **37**, 597–611, https://doi.org/10.1175/1520-0469(1980)037<0597:TMAMSA>2.0.CO;2.

Heymsfield, A. J., A. Bansemer, M. R. Poellot, and N. Wood, 2015: Observations of ice microphysics through the melting layer. *J. Atmos. Sci.*, **72**, 2902–2928, https://doi.org/10.1175/JAS-D-14-0363.1.

Heymsfield, G. M., L. Tian, L. Li, M. McLinden, and J. I. Cervantes, 2013: Airborne radar observations of severe hailstorms: Implications for future spaceborne radar. *J. Appl. Meteor. Climatol.*, **52**, 1851–1867, https://doi.org/10.1175/JAMC-D-12-0144.1.

Hobbs, P. V., T. J. Matejka, P. H. Herzegh, J. D. Locatelli, and R. A. J. Houze Jr., 1980: The mesoscale and microscale structure and organization of clouds and precipitation in midlatitude cyclones. I: A case study of a cold front. *J. Atmos. Sci.*, **37**, 568–596, https://doi.org/10.1175/1520-0469(1980)037<0568:TMAMSA>2.0.CO;2.

Hou, A. Y., and Coauthors, 2014: The Global Precipitation Measurement Mission. *Bull. Amer. Meteor. Soc.*, **95**, 701–722, https://doi.org/10.1175/BAMS-D-13-00164.1.

Houze, R. A. J., Jr., and Coauthors, 2017: The Olympic Mountains Experiment (OLYMPEX). *Bull. Amer. Meteor. Soc.*, **98**, 2167–2188, https://doi.org/10.1175/BAMS-D-16-0182.1.

Jensen, M. P., and Coauthors, 2016: The Midlatitude Continental Convective Clouds Experiment (MC3E). *Bull. Amer. Meteor. Soc.*, **97**, 1667–1686, https://doi.org/10.1175/BAMS-D-14-00228.1.

Katsumata, M., H. Uyeda, K. Iwanami, and G. Liu, 2000: The response of 36- and 89-GHz microwave channels to convective snow clouds over ocean: Observation and modeling. *J. Appl. Meteor. Climatol.*, **39**, 2322–2335, https://doi.org/10.1175/1520-0450(2000)039<2322:TROAGM>2.0.CO;2.

Keeler, J. M., B. F. Jewett, R. M. Rauber, G. M. McFarquhar, R. M. Rasmussen, L. Xue, C. Liu, and G. Thompson, 2016: Dynamics of cloud-top generating cells in winter cyclones. Part I: Idealized simulations in the context of field observations. *J. Atmos. Sci.*, **73**, 1507–1527, https://doi.org/10.1175/JAS-D-15-0126.1.

Kroodsma, R. A., M. A. Fritts, J. F. Lucey, M. R. Schwaller, T. J. Ames, C. M. Cooke, and L. M. Hillard, 2019: CoSMIR performance during the GPM OLYMPEX campaign. *IEEE Trans. Geosci. Remote Sens.*, **57**, 6397–6407, https://doi.org/10.1109/TGRS.2019.2906039.

Leinonen, J., and Coauthors, 2018: Retrieval of snowflake microphysical properties from multifrequency radar observations. *Atmos. Meas. Tech.*, **11**, 5471–5488, https://doi.org/10.5194/amt-11-5471-2018.

Leppert, K. D. I., and D. K. Cecil, 2015: Signatures of hydrometeor species from airborne passive microwave data for frequencies 10–183 GHz. *J. Appl. Meteor. Climatol.*, **54**, 1313–1334, https://doi.org/10.1175/JAMC-D-14-0145.1.

Li, H., and D. Moisseev, 2019: Melting layer attenuation at Ka- and W-bands as derived from multifrequency radar Doppler spectra observations. *J. Geophys. Res. Atmos.*, **124**, 9520–9533, https://doi.org/10.1029/2019JD030316.

——, J. Tiira, A. von Lerber, and D. Moisseev, 2020: Towards the connection between snow microphysics and melting layer: Insights from multifrequency and dual-polarization radar observations during BAECC. *Atmos. Chem. Phys.*, **20**, 9547–9562, https://doi.org/10.5194/acp-20-9547-2020.

Li, L., G. Heymsfield, L. Tian, and P. E. Racette, 2005: Measurements of ocean surface backscattering using an airborne 94-GHz cloud radar—Implication for calibration of airborne and spaceborne W-band radars. *J. Atmos. Oceanic Technol.*, **22**, 1033–1045, https://doi.org/10.1175/JTECH1722.1.

——, ——, J. Carswell, D. Schaubert, J. Creticos, and M. Vega, 2008: High-altitude imaging wind and rain airborne radar (HIWRAP). *IGARSS 2008—2008 IEEE Int. Geoscience and Remote Sensing Symp.*, Boston, MA, Institute of Electrical and Electronics Engineers, 354–357, https://doi.org/10.1109/IGARSS.2008.4779356.

——, and Coauthors, 2016: The NASA high-altitude imaging wind and rain airborne profiler. *IEEE Trans. Geosci. Remote Sens.*, **54**, 298–310, https://doi.org/10.1109/TGRS.2015.2456501.

Liao, L., and R. Meneghini, 2011: A study on the feasibility of dual-wavelength radar for identification of hydrometeor phases. *J. Appl. Meteor. Climatol.*, **50**, 449–456, https://doi.org/10.1175/2010JAMC2499.1.

——, ——, L. Tian, and G. M. Heymsfield, 2008: Retrieval of snow and rain from combined X- and W-band airborne radar measurements. *IEEE Trans. Geosci. Remote Sens.*, **46**, 1514–1524, https://doi.org/10.1109/TGRS.2008.916079.

——, ——, A. Tokay, and L. F. Bliven, 2016: Retrieval of snow properties for ku- and ka-band dual-frequency radar. *J. Appl. Meteor. Climatol.*, **55**, 1845–1858, https://doi.org/10.1175/JAMC-D-15-0355.1.

McFarquhar, G. M., M. S. Timlin, R. M. Rauber, B. F. Jewett, J. A. Grim, and D. P. Jorgensen, 2007: Vertical variability of cloud hydrometeors in the stratiform region of mesoscale convective systems and bow echoes. *Mon. Wea. Rev.*, **135**, 3405–3428, https://doi.org/10.1175/MWR3444.1.

McGaughey, G., E. J. Zipser, R. W. Spencer, and R. E. Hood, 1996: High-resolution passive microwave observations of convective systems over the tropical Pacific Ocean. *J. Appl. Meteor.*, **35**, 1921–1947, https://doi.org/10.1175/1520-0450(1996)035<1921:HRPMOO>2.0.CO;2.

McMurdie, L., G. Heymsfield, J. E. Yorks, and S. A. Braun, 2019: Investigation of Microphysics and Precipitation for Atlantic Coast-Threatening Snowstorms (IMPACTS) collection. NASA EOSDIS Global Hydrology Resource Center Distributed Active Archive Center, accessed 1 October 2020, https://doi.org/10.5067/IMPACTS/DATA101.

——, M. Miller, J. Munchak, B. Rauber, F. Waitz, G. Sova, T. Lang, and R. Kroodsma, 2020: Science summary for 1 February 2020: Warm developing oceanic frontal system in the southern Atlantic with a GPM overpass. IMPACTS, https://catalog.eol.ucar.edu/impacts_2020/showfile/85455245.

——, and Coauthors, 2022: Chasing snowstorms: The Investigation of Microphysics and Precipitation for Atlantic Coast-Threatening Snowstorms (IMPACTS) campaign. *Bull. Amer. Meteor. Soc.*, **103**, E1243–E1269, https://doi.org/10.1175/BAMS-D-20-0246.1.

Meneghini, R., H. Kim, L. Liao, J. A. Jones, and J. M. Kwiatkowski, 2015: An initial assessment of the surface reference technique applied to data from the dual-frequency precipitation radar (DPR) on the GPM satellite. *J. Atmos. Oceanic Technol.*, **32**, 2281–2296, https://doi.org/10.1175/JTECH-D-15-0044.1.

——, L. Liao, and G. M. Heymsfield, 2019: Attenuation correction over ocean for the HIWRAP dual-frequency airborne scatterometer. *J. Atmos. Oceanic Technol.*, **36**, 2015–2030, https://doi.org/10.1175/JTECH-D-19-0039.1.

Misumi, R., Y. Uji, and T. Maesaka, 2021: Modification of raindrop size distribution due to seeder–feeder interactions between stratiform precipitation and shallow convection observed by X-band polarimetric radar and optical disdrometer. *Atmos. Sci. Lett.*, **22**, e1034, https://doi.org/10.1002/asl.1034.

Ni, X., C. Liu, and E. Zipser, 2019: Ice microphysical properties near the tops of deep convective cores implied by the GPM dual-frequency radar observations. *J. Atmos. Sci.*, **76**, 2899–2917, https://doi.org/10.1175/JAS-D-18-0243.1.

Olson, W. S., C. D. Kummerow, G. M. Heymsfield, and L. Giglio, 1996: A method for combined passive-active microwave retrievals of cloud and precipitation profiles. *J. Appl. Meteor.*, **35**, 1763–1789, https://doi.org/10.1175/1520-0450(1996)035<1763:AMFCPM>2.0.CO;2.

Panegrossi, G., J.-F. Rysman, D. Casella, A. C. Marra, P. Sano, and M. S. Kulie, 2017: Cloudsat-based assessment of GPM microwave imager snowfall observation capabilities. *Remote Sens.*, **9**, 1263, https://doi.org/10.3390/rs9121263.

Pfaff, T., A. Engelbrecht, and J. Seidel, 2014: Detection of the bright band with a vertically pointing k-band radar. *Meteor. Z.*, **23**, 527–534, https://doi.org/10.1127/metz/2014/0605.

Piepmeier, J. R., P. Racette, W. Manning, and J. R. Wang, 2002: The airborne conical scanning millimeter-wave imaging radiometer (CoSMIR). *IEEE Int. Geoscience and Remote Sensing Symp.*, Toronto, ON, Canada, Institute of Electrical and Electronics Engineers, 783–785, https://doi.org/10.1109/IGARSS.2002.1025685.

Ramelli, F., and Coauthors, 2021: Microphysical investigation of the seeder and feeder region of an alpine mixed-phase cloud. *Atmos. Chem. Phys.*, **21**, 6681–6706, https://doi.org/10.5194/acp-21-6681-2021.

Rauber, R. M., M. K. Macomber, D. M. Plummer, A. A. Rosenow, G. M. McFarquhar, B. F. Jewett, D. Leon, and J. M. Keeler, 2014: Finescale radar and airmass structure of the comma head of a continental winter cyclone: The role of three airstreams. *Mon. Wea. Rev.*, **142**, 4207–4229, https://doi.org/10.1175/MWR-D-14-00057.1.

Reid, J. S., and Coauthors, 2023: The coupling between tropical meteorology, aerosol lifecycle, convection, and radiation, during the Cloud, Aerosol and Monsoon Processes Philippines Experiment (CAMP^{2}Ex). *Bull. Amer. Meteor. Soc.*, **104**, E1179–E1205, https://doi.org/10.1175/BAMS-D-21-0285.1.

Rosenow, A. A., D. M. Plummer, R. M. Rauber, G. M. McFarquhar, B. F. Jewett, and D. Leon, 2014: Vertical velocity and physical structure of generating cells and convection in the comma head region of continental winter cyclones. *J. Atmos. Sci.*, **71**, 1538–1558, https://doi.org/10.1175/JAS-D-13-0249.1.

Rutledge, S. A., and P. V. Hobbs, 1984: The mesoscale and microscale structure and organization of clouds and precipitation in midlatitude cyclones. XII: A diagnostic modeling study of precipitation development in narrow cold-frontal rainbands. *J. Atmos. Sci.*, **41**, 2949–2972, https://doi.org/10.1175/1520-0469(1984)041<2949:TMAMSA>2.0.CO;2.

Sadowy, G. A., 1999: A 95 GHz airborne cloud radar: Statistics of cloud reflectivity and analysis of beam-filling errors for a proposed spaceborne cloud radar. Ph.D. thesis, University of Massachusetts Amherst, 79 pp.

——, A. C. Berkun, W. Chun, E. Im, and S. L. Durden, 2003: Development of an advanced airborne precipitation radar. *Microwave J.*, **46**, 84–98.

Skofronick-Jackson, G., and B. T. Johnson, 2011: Surface and atmospheric contributions to passive microwave brightness temperatures for falling snow events. *J. Geophys. Res.*, **116**, D02213, https://doi.org/10.1029/2010JD014438.

——, and J. R. Wang, 2012: CoSMIR measurements in support of GPM algorithm development and validation. *2012 Fall Meeting*, San Francisco, CA, Amer. Geophys. Union, Abstract H31M-05.

——, B. T. Johnson, and S. J. Munchak, 2013: Detection thresholds of falling snow from satellite-borne active and passive sensors. *IEEE Trans. Geosci. Remote Sens.*, **51**, 4177–4189, https://doi.org/10.1109/TGRS.2012.2227763.

Spencer, R. W., R. E. Hood, F. J. Lafontaine, E. A. Smith, R. Platt, J. Galliano, V. L. Griffin, and E. Lobl, 1994: High-resolution imaging of rain systems with the advanced microwave precipitation radiometer. *J. Atmos. Oceanic Technol.*, **11**, 849–857, https://doi.org/10.1175/1520-0426(1994)011<0849:HRIORS>2.0.CO;2.

Stark, D., B. A. Colle, and S. E. Yuter, 2013: Observed micro-
physical evolution for two East Coast winter storms and the
associated snow bands. *Mon. Wea. Rev.*, **141**, 2037–2057,
https://doi.org/10.1175/MWR-D-12-00276.1.

Tanelli, S., S. L. Durden, and E. Im, 2006: Simultaneous measure-
ments of ku- and ka-band sea surface cross sections by an air-
borne radar. *IEEE Geosci. Remote Sens. Lett.*, **3**, 359–363,
https://doi.org/10.1109/LGRS.2006.872929.

Tian, L., G. M. Heymsfield, A. C. J. Didlake Jr., S. Guimond, and
L. Li, 2015: Velocity–azimuth display analysis of Doppler
velocity for HIWRAP. *J. Appl. Meteor. Climatol.*, **54**, 1792–
1808, https://doi.org/10.1175/JAMC-D-14-0054.1.

Tyynelä, J., and V. Chandrasekar, 2014: Characterizing falling
snow using multifrequency dual-polarization measurements.
J. Geophys. Res. Atmos., **119**, 8268–8283, https://doi.org/10.
1002/2013JD021369.

Vivekanandan, J., J. Turk, and V. N. Bringi, 1993: Comparisons of
precipitation measurements by the advanced microwave precipi-
tation radiometer and multiparameter radar. *IEEE Trans. Geosci.
Remote Sens.*, **31**, 860–870, https://doi.org/10.1109/36.239909.